

A Parallel Low-Rank Solver for the Six-Dimensional Vlasov-Maxwell Equations

F. Allmann-Rahn^{a,*}, R. Grauer^a, K. Kormann^b

^a*Ruhr University Bochum, Universitätsstraße 150, 44801 Bochum, Germany*

^b*Uppsala University, P.O. Box 256, SE-751 05 Uppsala, Sweden*

Abstract

Continuum Vlasov simulations can be utilized for highly accurate modelling of fully kinetic plasmas. Great progress has been made recently regarding the applicability of the method in realistic plasma configurations. However, a reduction of the high computational cost that is inherent to fully kinetic simulations would be desirable, especially at high velocity space resolutions. For this purpose, low-rank approximations can be employed. The so far available low-rank solvers are restricted to either electrostatic systems or low dimensionality and can therefore not be applied to most space, astrophysical and fusion plasmas. In this paper we present a new parallel low-rank solver for the full six-dimensional electromagnetic Vlasov-Maxwell equations with a compression of the particle distribution function in velocity space. Special attention is paid to mass conservation and Gauss's law. The low-rank Vlasov solver is applied to standard benchmark problems of plasma turbulence and magnetic reconnection and compared to the full grid method. It yields accurate results at significantly reduced computational cost.

Keywords: Vlasov simulation, kinetic plasmas, low-rank approximation, hierarchical Tucker decomposition, tensor networks

1. Introduction

Fully kinetic continuum Vlasov simulations feature a highly accurate representation of velocity space and are utilized in the modelling of plasmas with great success (e.g. [1, 2, 3, 4, 5, 6]).

One remaining issue is that the possible resolutions are still very limited, since computations involve the six-dimensional plasma distribution function. In order to reduce computational cost and reach higher resolutions, low-rank techniques have been introduced to plasma physics in Kormann (2015) [7] where

*Corresponding author

Email address: far@tp1.rub.de (F. Allmann-Rahn)

the discretized plasma distribution function is approximated by a tensor of low rank. This approximation can be considered a compression of the distribution function with both lossy and lossless elements. The distribution function is decomposed by means of singular value decompositions (SVDs) and the information associated with small singular values is discarded. The lossless aspect of the compression results from the exploitation of separability.

In general, low-rank techniques have become very popular in the last years in many areas of physics, mathematics, computer science and more (see e.g. [8, 9, 10, 11] and references therein). In plasma physics and hydrodynamics different approaches to adapting tensor compression have been developed. The approach from Ehrlacher & Lombardi (2017) [12] starts from the Hamiltonian formulation of the Vlasov-Poisson system to find a natural splitting for the low-rank approximation. They use the proper generalized decomposition (PGD) where the alternating least squares (ALS) optimization method is employed to find the low-rank tensor. This is in contrast to SVD-based low-rank approximations where no optimization problem is solved. In both [7] and [12] the high-dimensional computations from usual Vlasov schemes are replaced by computations in low-rank format. During each mathematical operation, the rank increases and is truncated back to lower rank. A different method is introduced in Einkemmer & Lubich (2018) [13] for the Vlasov-Poisson system. They apply a dynamical low-rank approximation where the Vlasov equation is projected to a low-rank manifold so that all computations are done within this manifold and the rank does not increase by the computations. Position space and velocity space are decomposed so that the six-dimensional problem is reduced to two three-dimensional advection problems times the rank. Alternatively, the six-dimensional advection is split up into six one-dimensional advection problems times the rank. The method is extended in [14] to conserve mass, momentum and energy making use of a Lagrange-multiplier technique to enforce the conservation properties. An extension from the electrostatic system to the 1D2V Vlasov-Maxwell system is given in [15]. The Vlasov-Poisson version of the code is ported to graphics processing units (GPUs) in [16]. As in plasma physics, low-rank algorithms can also be utilized in the related field of hydrodynamics. Dolgov and Stoll (2017) [17] apply low-rank approximations to the optimization problems in the solution of Navier-Stokes equations. Fluid dynamics can also utilize the Boltzmann equation with a collision term which is done by means of low-rank decompositions in Einkemmer (2019) [18].

The aforementioned low-rank Vlasov solvers are restricted to the electrostatic Vlasov-Poisson system or in one case the electromagnetic Vlasov-Maxwell system in one spatial dimension and two velocity dimensions. Therefore, they cannot yet be applied to many of the physical problems arising for example in space and astrophysics or in fusion research. In this paper we present a new parallel low-rank solver for the full six-dimensional electromagnetic Vlasov-Maxwell system. We build upon the earlier work in [7], but choose to compress only the velocity space using the hierarchical Tucker decomposition [19, 20]. There are multiple advantages with this approach as will be discussed in the next section, most prominently this enables us to parallelize our algorithm for use on large

high performance computing systems.

2. Vlasov-Maxwell Equations and Low-Rank Decomposition

A plasma is accurately characterized by six-dimensional phase-space distribution functions. For numerical modelling we consider the positional coordinate $\mathbf{x} \in \Omega_x \subset \mathbb{R}^3$ and the velocity coordinate $\mathbf{v} \in \Omega_v \subset \mathbb{R}^3$ so that $\Omega_x \times \Omega_v$ is a subset of the phase space, and a time $t \in [0, \tau_{\max}]$. Then the distribution function is $f_s(\mathbf{x}, \mathbf{v}, t) : \Omega_x \times \Omega_v \times [0, \tau_{\max}] \rightarrow \mathbb{R}$ for each particle species s . The particle motion in the collisionless case is governed by the Vlasov equation

$$\frac{\partial f_s(\mathbf{x}, \mathbf{v}, t)}{\partial t} + \mathbf{v} \cdot \nabla f_s(\mathbf{x}, \mathbf{v}, t) + \frac{q_s}{m_s} (\mathbf{E}(\mathbf{x}, t) + \mathbf{v} \times \mathbf{B}(\mathbf{x}, t)) \cdot \nabla_v f_s(\mathbf{x}, \mathbf{v}, t) = 0 \quad (1)$$

with the electric field \mathbf{E} and the magnetic field \mathbf{B} . Together with Maxwell's equations

$$\begin{aligned} \nabla \cdot \mathbf{E}(\mathbf{x}, t) &= \frac{\rho(\mathbf{x}, t)}{\epsilon_0}, \quad \nabla \cdot \mathbf{B}(\mathbf{x}, t) = 0, \\ \nabla \times \mathbf{E}(\mathbf{x}, t) &= -\frac{\partial \mathbf{B}(\mathbf{x}, t)}{\partial t}, \quad \nabla \times \mathbf{B}(\mathbf{x}, t) = \mu_0 \mathbf{j}(\mathbf{x}, t) + \mu_0 \epsilon_0 \frac{\partial \mathbf{E}(\mathbf{x}, t)}{\partial t} \end{aligned} \quad (2)$$

the Vlasov equation provides a complete plasma description. The charge and current densities are denoted by ρ and \mathbf{j} , and μ_0, ϵ_0 are the vacuum permeability and the vacuum permittivity, respectively.

Plasma quantities in position space can be derived from the distribution function by taking moments, i.e. multiplying f_s by powers of \mathbf{v} and taking the integral over velocity space. The zeroth moment, the particle density is $n_s(\mathbf{x}, t) = \int f_s(\mathbf{x}, \mathbf{v}, t) d\mathbf{v}$ and the mean velocity (derived from the first moment) is $\mathbf{u}_s(\mathbf{x}, t) = \frac{1}{n_s(\mathbf{x}, t)} \int \mathbf{v} f_s(\mathbf{x}, \mathbf{v}, t) d\mathbf{v}$. The second moment (multiplied by mass) is given by $\mathcal{P}_s(\mathbf{x}, t) = m_s \int \mathbf{v} \otimes \mathbf{v} f_s(\mathbf{x}, \mathbf{v}, t) d\mathbf{v}$, where \otimes denotes the Kronecker product. The charge and current densities can be obtained from the moments as $\rho(\mathbf{x}, t) = \sum_s q_s n_s(\mathbf{x}, t)$ and $\mathbf{j}(\mathbf{x}, t) = \sum_s q_s n_s(\mathbf{x}, t) \mathbf{u}_s(\mathbf{x}, t)$. Temperature T is related to the raw second moment \mathcal{P} like $T = (\mathcal{P} - mn \mathbf{u} \otimes \mathbf{u}) / (nk_B)$. Taking the zeroth moment and the first moment of the complete Vlasov equation leads to two fluid equations, the continuity equation for particle density

$$\frac{\partial n_s(\mathbf{x}, t)}{\partial t} + \nabla \cdot (n_s(\mathbf{x}, t) \mathbf{u}_s(\mathbf{x}, t)) = 0, \quad (3)$$

and the momentum equation

$$m_s \frac{\partial (n_s(\mathbf{x}, t) \mathbf{u}_s(\mathbf{x}, t))}{\partial t} = n_s q_s (\mathbf{E}(\mathbf{x}, t) + \mathbf{u}_s(\mathbf{x}, t) \times \mathbf{B}(\mathbf{x}, t)) - \nabla \cdot \mathcal{P}_s(\mathbf{x}, t). \quad (4)$$

Higher moments of the Vlasov equation yield further equations and this hierarchy forms the full set of fluid equations. The hierarchy is exact but any finite truncation is not closed because the equation for one moment always includes the next higher moment. Considering only the first two fluid equations,

one is missing an equation for \mathcal{P}_s . In Sec. 3.6 we will obtain \mathcal{P}_s from the distribution function in order to close the system and get exact kinetic results for n_s and \mathbf{u}_s .

In this paper we present a solver for the Vlasov equation (1) that makes use of low-rank approximations. There, the central operation is the singular value decomposition (SVD), since a truncated singular value decomposition based on the r largest singular values corresponds to the best rank- r approximation in the Frobenius norm and other norms that are invariant under unitary transformations [21, 22, 23]. If the singular values decay fast, the SVD provides a very efficient approximation in the sense that a sufficiently exact reconstruction can be made although only the most important information (contained in the large singular values) was kept. This can be thought of as a lossy compression of the matrix.

There is also a loss-free aspect of this matrix compression as the SVD is an efficient representation of separable matrices. In the low-rank Vlasov solver this property is exploited, for example distribution functions that are close to Maxwellian can be represented with small ranks. A plasma is typically Maxwell distributed in calm or collision-dominated regions. The Maxwell distribution separates in velocity space like $f_{\text{Maxwell}}(\mathbf{x}, \mathbf{v}) = f_1(\mathbf{x}, v_x) f_2(\mathbf{x}, v_y) f_3(\mathbf{x}, v_z)$, where f_i , $i \in \{1, 2, 3\}$, is a normal distribution with an expectation value of $\mu_i(\mathbf{x}) = u_i(\mathbf{x})$ and a standard deviation of $\sigma(\mathbf{x}) = \sqrt{\frac{k_B T_s(\mathbf{x})}{m_s}}$. The separable Maxwell distribution is of rank one in velocity space and can therefore be compressed very well. If three-dimensional velocity space Ω_v at position \mathbf{x} is represented by a grid with C cells in each velocity direction, a Maxwellian distribution is fully represented by $3C$ instead of C^3 values. This is a strong motivation for using low-rank approximations to speed up computations that involve the plasma distribution function.

3. Low-Rank Vlasov Solver

3.1. Hierarchical Tucker Decomposition of the Distribution Function

Numerical Vlasov solvers discretize the particle distribution function on a six-dimensional phase space grid so that each cell in the grid corresponds to a value of f at a phase space point (x, y, z, v_x, v_y, v_z) (or the average value of f in the cell around that point). The discretized f can be considered a sixth order tensor and low-rank tensor decomposition techniques can be applied to f . In the previous section the low-rank decomposition of a matrix was discussed. The concept can be generalized to tensors in various ways, for example in the form of the higher-order singular value decomposition/Tucker decomposition, the tensor train decomposition/matrix product states, or the hierarchical Tucker decomposition (HTD). Here, the hierarchical Tucker decomposition is chosen for the low-rank approximation of f . It is computed by constructing matricizations (also called flattenings) of the tensor that is supposed to be decomposed. A matricization of the distribution function $\mathbf{f} \in \mathbb{R}^{N_x \times N_{v_x} \times N_y \times N_{v_y} \times N_z \times N_{v_z}}$ can for example be the matrix $M \in \mathbb{R}^{N_x N_{v_x} \times N_y N_{v_y} N_z N_{v_z}}$. Naturally, it is possible to

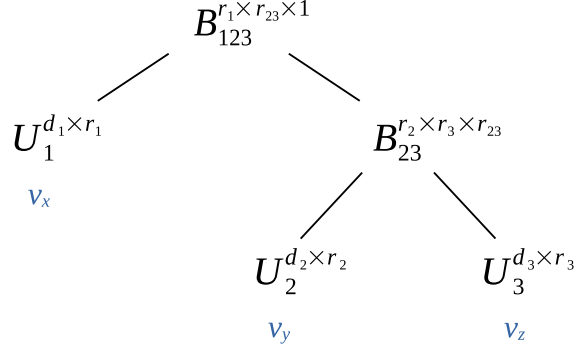


Figure 1: At each coordinate (x, y, z) the velocity distribution $f(v_x, v_y, v_z)$ is decomposed according to the shown hierarchical Tucker tree. The coordinates which the respective factor matrices belong to are highlighted in blue.

choose different ways to combine the dimensions in order to obtain a matrix. This choice determines the tree structure of the HTD. To a matricization and its transpose the singular value decomposition can be applied. Matrices that are part of the decomposition are then rearranged to different matricizations and again SVDs are applied. This procedure is repeated hierarchically. The computation of the HTD and mathematical operations in HT format are described in the original papers by Hackbusch & Kühn [19] and Grasedyck [20]. Detailed information on the implementation in computer programs is given by Tobler and Kressner [24, 25].

When the low-rank method was first used for the electrostatic Vlasov equation in [7], the choice was to apply a tensor train decomposition to the six-dimensional distribution function $f(x, y, z, v_x, v_y, v_z)$ to compress the full phase space information. This approach can be extended to the Vlasov-Maxwell equations. However, it is so far not possible to efficiently parallelize a Vlasov solver where all six dimensions of the distribution function are compressed. Combined with the fact that high ranks are necessary to represent large-scale physical configurations, the applicability of such a solver for realistic physical problems is very limited. There are several reasons why it is favourable to compress only the velocity space at each point (x, y, z) and keep the grid in position space. Due to the separability of a Maxwellian distribution, velocity space is expected to compress well and the worst case of rank one is still physically sensible. There is more freedom in the choice of advection schemes which is important for numerical stability. In the case of compression in all six dimensions, element-wise products in hierarchical Tucker format would need to be performed, whereas computationally cheaper additions are sufficient when only velocity space is compressed. Finally, efficient parallelization by means of a domain decomposition approach in position space is straightforward.

The hierarchical Tucker tree of the distribution function is shown in Fig. 1 in the form that we use. It consists of factor matrices $U_i \in \mathbb{R}^{N_i \times r_i}$ where

N_i is the number of velocity space cells and r_i is the rank in each direction $i \in \{1, 2, 3\}$. They are connected via the transfer tensors $B_{23} \in \mathbb{R}^{r_2 \times r_3 \times r_{23}}$ and $B_{123} \in \mathbb{R}^{r_1 \times r_{23} \times 1}$. For each point of the grid in position space, indexed by $\mathbf{i} = (i_1, i_2, i_3)$, we have a hierarchical Tucker tensor of the form

$$\text{vec}(f(x_{i_1}, y_{i_2}, z_{i_3}, :, :, :)) = ((U_3^{\mathbf{i}} \otimes U_2^{\mathbf{i}}) B_{23}^{\mathbf{i}} \otimes U_1^{\mathbf{i}}) B_{123}^{\mathbf{i}}. \quad (5)$$

The original motivation for choosing the hierarchical Tucker decomposition over the HOSVD/Tucker decomposition or tensor trains was that in the compression of the full six-dimensional phase space, the ordering of dimensions in the tensor train format is unintuitive [7] whereas the HOSVD has a high-dimensional core tensor. In the new approach of compressing only velocity space, the HTD can be exchanged with the HOSVD or tensor trains with no major differences in the level of compression to be expected. One advantage of the HTD may be that many plasma configurations feature different physics in one direction (e.g. due to a magnetic guide field) so that the HTD with one singled out direction can be a natural representation. However, thorough tests would be necessary to find out which type of decomposition is best suited for the respective physical configurations and the differences are expected to be small.

The tree shown in Fig. 1 can also be used for a one- or two-dimensional velocity space by setting the numbers of cells, ranks and values in the factor matrices U of one or two dimensions to one. In a typical application, the ranks r and the numbers of cells N in each velocity direction are fixed so that for three-dimensional velocity space the compression C is given by $C = (3Nr + r^3 + r^2)/N^3$.

Low-rank Vlasov simulations can utilize such high resolutions that the uncompressed distribution function may not fit into memory or be too costly to compute. For this reason it is preferred to provide the initial configuration directly in the low-rank form instead of initializing the full distribution function and then truncating it. Fortunately plasma simulations are often initialized with Maxwellian distributions which can be directly set in hierarchical Tucker format. For this purpose, a hierarchical Tucker tensor is initialized with ranks one and all transfer tensors and factor matrices set to one. Then the root tensor of $f(\mathbf{x}) \in \mathbb{H}$ (denoting the set of hierarchical Tucker tensors by \mathbb{H}) is responsible for the normalization

$$(B_{123})_{11} = n(\mathbf{x}) \left(\frac{m}{2\pi T(\mathbf{x})} \right)^{d/2} \quad (6)$$

with dimensionality of velocity space d . The factor matrices represent the exponential distribution as

$$(U_i)_{k1} = \exp \left(-\frac{m}{2T(\mathbf{x})} ((v_i)_k - u_i(\mathbf{x}))^2 \right) \quad \forall 1 \leq i \leq d \in \mathbb{N}, \quad k \in \{1, \dots, N_i\} \quad (7)$$

with $(v_i)_k = v_{i,\text{begin}} + (k - 1/2)\Delta v_i$.

3.2. Computing Moments

Low-rank decompositions are sometimes also called *tensor networks* because they decompose a large tensor into multiple smaller tensors that are connected with each other. The connection can be resolved by contractions of the multiple small tensors to again yield one large tensor. The contraction of, for example, two third-order tensors $A \in \mathbb{C}^{\alpha_1 \times \alpha_2 \times \alpha_3}$ and $B \in \mathbb{C}^{\beta_1 \times \beta_2 \times \beta_3}$ in the modes α_3 and β_1 is denoted as $A \circ_{3,1} B$ and can be thought of as the inner product in these modes:

$$(A \circ_{3,1} B)_{i_1, i_2, j_2, j_3} = \sum_{s=1}^{\alpha_3} A_{i_1, i_2, s} B_{s, j_2, j_3} \quad (8)$$

with $A \circ_{3,1} B \in \mathbb{C}^{\alpha_1 \times \alpha_2 \times \beta_2 \times \beta_3}$. This implies that modes α_3 and β_1 must be of equal size. Similar to Einstein notation, we will sometimes assume contractions over identical modes when it is clear from the context or explicitly mentioned.

Moments of the compressed distribution function can be obtained by first contracting the factor matrices U with vectors that represent the velocity space discretization. Then the results of the contractions are contracted with the transfer tensors B . This procedure can also be thought of as the implementation of the contraction of the hierarchical Tucker tensor with a vector.

Let $\mathbf{V}_i^k \in \mathbb{R}^{N_i}$ be a vector that represents the discretization in velocity space (to the power k) in direction $i \in \{1, 2, 3\}$ and has elements

$$(V_i^k)_j = \left(v_{i, \text{begin}} + \left(j - \frac{1}{2} \right) \Delta v_i \right)^k \Delta v_i, \quad j \in \{1, \dots, N_i\}, \quad (9)$$

where $v_{i, \text{begin}}$ is the lower limit of the discrete velocity space and Δv_i is the cell size in direction i . These vectors can be contracted with the factor matrices to yield vectors

$$\mathbf{U}_i^k = \mathbf{V}_i^k \circ_{1,1} U_i \in \mathbb{R}^{r_i}, \quad i \in \{1, 2, 3\} \quad (10)$$

which are then contracted with the transfer tensors. The first moment of the distribution function is given by

$$n = (\mathbf{U}_3^0 \circ_{1,1} (\mathbf{U}_2^0 \circ_{1,1} B_{23})) \circ_{1,1} (\mathbf{U}_1^0 \circ_{1,1} B_{123}). \quad (11)$$

A different notation with implicit contractions over identical modes is

$$n = \mathbf{U}_3^0 \text{ }^{r_3} \mathbf{U}_2^0 \text{ }^{r_2} B_{23}^{r_2 \times r_3 \times r_{23}} \mathbf{U}_1^0 \text{ }^{r_1} B_{123}^{r_1 \times r_{23} \times 1}. \quad (12)$$

For better readability the tensor dimensions are omitted and the directions are denoted by $\{x, y, z\}$ instead of $\{1, 2, 3\}$ so that (11) is shortly written as

$$n = \mathbf{U}_z^0 \mathbf{U}_y^0 B_{23} \mathbf{U}_x^0 B_{123}. \quad (13)$$

With this notation, higher moments are given by

$$\begin{aligned} u_x n &= \mathbf{U}_z^0 \mathbf{U}_y^0 B_{23} \mathbf{U}_x^1 B_{123}, & u_y n &= \mathbf{U}_z^0 \mathbf{U}_y^1 B_{23} \mathbf{U}_x^0 B_{123}, \\ u_z n &= \mathbf{U}_z^1 \mathbf{U}_y^0 B_{23} \mathbf{U}_x^0 B_{123}, \end{aligned} \quad (14)$$

and

$$\mathcal{P}_{xx} = \mathbf{U}_z^0 \mathbf{U}_y^0 \mathbf{B}_{23} \mathbf{U}_x^2 \mathbf{B}_{123}, \quad \mathcal{P}_{xy} = \mathbf{U}_z^0 \mathbf{U}_y^1 \mathbf{B}_{23} \mathbf{U}_x^1 \mathbf{B}_{123}, \quad \dots \quad (15)$$

and

$$\begin{aligned} \mathcal{Q}_{xxx} &= \mathbf{U}_z^0 \mathbf{U}_y^0 \mathbf{B}_{23} \mathbf{U}_x^3 \mathbf{B}_{123}, & \mathcal{Q}_{xxy} &= \mathbf{U}_z^0 \mathbf{U}_y^1 \mathbf{B}_{23} \mathbf{U}_x^2 \mathbf{B}_{123}, & \dots \\ \mathcal{Q}_{xyz} &= \mathbf{U}_z^1 \mathbf{U}_y^1 \mathbf{B}_{23} \mathbf{U}_x^1 \mathbf{B}_{123}, & \dots \end{aligned} \quad (16)$$

The computation of moments in the presented way utilizes the midpoint rule for the integration over velocity space.

3.3. Split-step semi-Lagrangian scheme

Semi-Lagrangian algorithms discretize the distribution function on a grid, solve the characteristics backward in time for the grid points and interpolate the value at the foot of the characteristics from the values at the grid points for the previous time steps. It is common to apply an operator splitting between the \mathbf{x} and \mathbf{v} advection steps. In the second-order time splitting that we use, a half velocity space step (using $\Delta t/2$ for the update) is followed by a full step in position space and a second half step in velocity space. This is also known as the leapfrog method. Moreover, the \mathbf{x} and \mathbf{v} advection steps are further split into three one-dimensional advection steps. The advantage of such a splitting is that the advection coefficients are then independent of the advection direction and thus the characteristics are simple.

Many of the available semi-Lagrangian interpolation methods (e.g. Lagrangian interpolation or spline interpolation) are applicable in the context of a low-rank Vlasov solver. In this paper, we use the positive and flux-conservative (PFC) method from [26] without limiters, since this method leads to relatively few numerical oscillations. We simplify the weights from the original PFC scheme in order to make them applicable in the low-rank solver. It is not yet clear how the slope limiters for preserving the positivity of the distribution function are efficiently applied when f is in a low-rank format because the cells that are arguments of the minimum function in the limiter are not explicitly available. Therefore, the limiters are for now turned off ($\epsilon^+ = \epsilon^- = 1$). This issue persists for all typical slope limiters, and it is clear that it is non-trivial to prevent negative values of the distribution function when it is not known which cells actually violate the positivity.

Before explaining how the PFC scheme can be implemented for a low-rank representation of the form (5), let us briefly recall the PFC scheme. We will focus on the one-dimensional case, since we split the steps into one-dimensional interpolations. We consider the equation

$$\partial_t f(t, x) + a \partial_x f(t, x) = 0, \quad (17)$$

for $a \in \mathbb{R}$ independent of x and t .

In the PFC scheme the grid points are not associated with the value of f at that certain point but with the average of f in the respective cell (or the

cell integral). Then the semi-Lagrangian method can be formulated in terms of fluxes in and out of the cell. Thus, f_i is now the average value of f within cell i which is given by

$$f_i^n = \frac{1}{\Delta x} \int_{x_{i-1/2}}^{x_{i+1/2}} f(t^n, x) dx. \quad (18)$$

The semi-Lagrangian update of the cell integral is

$$\int_{x_{i-1/2}}^{x_{i+1/2}} f(t^{n+1}, x) dx = \int_{X(x_{i-1/2})}^{X(x_{i+1/2})} f(t^n, x) dx \quad (19)$$

where X is the origin of the particle trajectory and $x_{i-1/2} = x_{\text{begin}} + (i-1) \Delta x$ is the left border of the i th cell with x_{begin} the lower limit in x -direction. For equation (17), this is given by $X(x_{i-1/2}) = x_{i-1/2} - a\Delta t$. The flux out of the cell is defined as

$$\Phi_{i+1/2}(t^n) = \int_{X(x_{i-1/2})}^{x_{i+1/2}} f(t^n, x) dx \quad (20)$$

so that the semi-Lagrangian update can be written as

$$\int_{x_{i-1/2}}^{x_{i+1/2}} f(t^{n+1}, x) dx = \Phi_{i-1/2}(t^n) + \int_{x_{i-1/2}}^{x_{i+1/2}} f(t^n, x) dx - \Phi_{i+1/2}(t^n). \quad (21)$$

Let us define $\alpha_i = \frac{X(x_{i+1/2}) - x_{j-1/2}}{\Delta x}$, where $j = i + \text{floor}\left(\frac{X(x_{i+1/2}) - x_{i-1/2}}{\Delta x}\right)$ is the index of the cell where $X(x_{i+1/2})$ is located. Then, the interpolation weights are computed as functions of the parameter α_i . For example for a third order interpolation stencil, the weights are then given by

$$\begin{aligned} w_{-1}^i &= -\alpha_i (1 - \alpha_i) (2 - \alpha_i) / 6 \\ w_0^i &= \begin{cases} (1 - \alpha_i) (1 - \alpha_i (2 - \alpha_i) / 6 + \alpha_i (1 + \alpha_i) / 6) & \alpha > 0 \\ -\alpha_i (1 - (1 - \alpha_i) (2 - \alpha_i) / 6 + (1 - \alpha_i) (1 + \alpha_i) / 6) & \alpha < 0. \end{cases} \\ w_1^i &= \alpha_i (1 - \alpha_i) (1 + \alpha_i) / 6. \end{aligned} \quad (22)$$

and the flux is given by

$$\Phi_{i+1/2} = f_{j-1}^n w_{-1}^i + f_j^n w_0^i + f_{j+1}^n w_1^i.$$

Note that the index i of the weights can be dropped, if α is independent of the index i which is the case when the advection coefficient (that determines α_i) is constant along the advection direction. This is the case for our split-step Vlasov solver.

3.4. Step in Position Space

First, we discuss the \mathbf{x} advection, i.e. we solve the equation

$$\partial_t f + \mathbf{v} \cdot \nabla_{\mathbf{x}} f = 0. \quad (23)$$

Denoting the value of f at time t^n by f^n and the new value at time $t^{n+1} = t^n + \Delta t$ by f^{n+1} it is

$$f^{n+1}(\mathbf{x}, \mathbf{v}) = f^n(\mathbf{x} - \mathbf{v}\Delta t, \mathbf{v}). \quad (24)$$

We can further split this into three one-dimensional advection problems. Let us exemplify the steps for the case of the first direction x . In this case, the normalized advection velocity is $\frac{x_{i-1/2} - X(x_{i+1/2})}{\Delta x} = -\frac{\Delta t v_1}{\Delta x}$. Hence, α and thus the weights are depending on the first velocity dimension only. Let us denote by \mathbf{i} the three-index in position space and by \mathbf{k} the three-index in velocity space. Then the flux is given by

$$\Phi_{i_1+1/2, i_2, i_3, \mathbf{k}} = f_{j-1, i_2, i_3, \mathbf{k}}^{n-1} w_{-1}(\alpha_{k_1}) + f_{j, i_2, i_3, \mathbf{k}}^n w_0(\alpha_{k_1}) + f_{j+1, i_2, i_3, \mathbf{k}}^{n+1} w_1(\alpha_{k_1}). \quad (25)$$

Note that the index j depends on the v_1 coordinate, i.e. on k_1 for the discretization. Hence, the dependence the expression (25) for the flux on k_1 is twofold: by the shift in index i_1 and the dependence of the weights. In order to split the dependence of the operator into a sum of Kronecker product operations, we want to construct weight vectors $W_\ell \in \mathbb{R}^{N_4}$, where N_4 is the number of grid points along v_1 , such that the flux vector can be constructed as

$$\Phi = \sum_{\ell} S_{\ell}^1(f) \star_4 W_{\ell}. \quad (26)$$

Here, \star_4 denotes the Hadamard product along direction 4. S_{ℓ}^1 denotes the operation shifting the first index by ℓ , i.e.

$$(S_{\ell}^1(f))_{\mathbf{ik}} = f_{\mathbf{i}+(\ell, 0, 0), \mathbf{k}}.$$

This operations has to be closed by suitable boundary conditions – we use a cyclic index shifting that corresponds to periodic boundary conditions.

If we assume that the advection velocity is limited by one cell size, we only have to consider the two cases $j = -1, 0$ for positive or negative velocities respectively. For the three-point stencil, this yields four weight vectors with the following entries for positive velocities (α negative)

$$\begin{aligned} w_{-2}^{k_1} &= 0, \\ w_{-1}^{k_1} &= -\alpha_{k_1} (1 - \alpha_{k_1}) / 6 \\ w_0^{k_1} &= (1 - \alpha_{k_1}) (1 - \alpha_{k_1} (2 - \alpha_{k_1}) / 6 + \alpha_{k_1} (1 + \alpha_{k_1}) / 6) \\ w_1^{k_1} &= \alpha_{k_1} (1 - \alpha_{k_1}) (1 + \alpha_{k_1}) / 6. \end{aligned} \quad (27)$$

and the following entries for negative velocities

$$\begin{aligned} w_{-2}^{k_1} &= -\alpha_{k_1} (1 - \alpha_{k_1}) (2 - \alpha_{k_1}) / 6 \\ w_{-1}^{k_1} &= \alpha_{k_1} (1 - (1 - \alpha_{k_1}) (2 - \alpha_{k_1}) / 6 + (1 - \alpha_{k_1}) (1 + \alpha_{k_1}) / 6) \\ w_0^{k_1} &= \alpha_{k_1} (1 - \alpha_{k_1}) (1 + \alpha_{k_1}) / 6, \\ w_1^{k_1} &= 0. \end{aligned} \quad (28)$$

If we want to allow for larger shifts, additional weight functions are necessary. In our implementation, we limit the shift to one cell in position space, since the time step restrictions are more severe for the step in velocity space in typical applications of the low-rank Vlasov solver.

A generalization of the method to a distribution function compressed in the form (5) is straight-forward: The index shift is applied in x direction where no compression is applied and the Hadamard product along mode 4 can be implemented by multiplying each column of the leaf matrix U_4 element-wise by the vector W_ℓ .

In this case four weights can be computed once initially for all velocity space cells, as they do not change with time. Then in every spatial step in direction x_j the neighbouring weighted hierarchical Tucker tensors $S_{-2}^1(f)W_{-2} \dots S_1^1(f)W_1$ are added up with a truncation in between each addition to compute the fluxes. Afterwards the new value of f can be obtained as

$$f_i^{n+1} = \Phi_{i-1/2} + f^n - \Phi_{i+1/2} \quad (29)$$

which again is a sum of HT tensors with a truncation after each addition.

3.5. Step in Velocity Space

The step in velocity space is given by the equation

$$\partial_t f + \frac{q}{m} (\mathbf{E} + \mathbf{v} \times \mathbf{B}) \cdot \nabla_{\mathbf{v}} f = 0. \quad (30)$$

so that

$$f^{n+1}(\mathbf{x}, \mathbf{v}) = f^n \left(\mathbf{x}, \mathbf{v} - \frac{q}{m} (\mathbf{E} + \mathbf{v} \times \mathbf{B}) \right). \quad (31)$$

The three-dimensional advection in velocity space can also be split up into one-dimensional advections. However, the Lorentz acceleration depends on velocity so that a symplectic second-order sequence for a velocity space step is $\frac{1}{2}$ step $v_x \rightarrow \frac{1}{2}$ step $v_y \rightarrow 1$ step $v_z \rightarrow \frac{1}{2}$ step $v_y \rightarrow \frac{1}{2}$ step v_x (Strang splitting). Due to the vector product, the components of the advection coefficient do only depend on the other two velocity directions and the position, for example $a_x = a_x(\mathbf{x}, v_y, v_z)$. For a similar construction as for the position space update, the weights for the one-dimension directions are now not only dependent one variable of the grid but on two, so the weights are matrices and not vectors anymore. In order to avoid the additional costs related to this dependence, we further split the velocity update into two subsequent advection steps, each depending only on one velocity space direction. At the example of the v_x -step the two advection velocities are

$$a_{x,1} = -\frac{q}{m} (E_x/2 + v_y B_z) \Delta t / \Delta v_x \quad (32)$$

and

$$a_{x,2} = -\frac{q}{m} (E_x/2 - v_z B_y) \Delta t / \Delta v_x. \quad (33)$$

Splitting up the advection is possible because it is a linear operation with no dependence on the updated velocity direction. Now the weights again correspond

to vectors and the strategy used for the step in position space can be applied. The acceleration due to the electric field has been evenly distributed between the two substeps which reduces time step restrictions for large electric fields and can prevent small advection velocities in the case of vanishing $(\mathbf{v} \times \mathbf{B})_j$. In principle, the velocity space update can also be conducted using a single advection step, but then the weights must be constructed in hierarchical Tucker format and the multiplication of f with the weights is an element-wise multiplication of two hierarchical Tucker tensors. This results in additional truncations or increased computational cost.

Let us now consider the construction of the flux for the advection by the advection velocity (32). Since we have a full grid in position space, we can consider the hierarchical Tucker tensor for each of these grid points separately

$$\Phi_{\mathbf{i}} = \sum_{\ell} S_{\ell}^4(f_{\mathbf{i}}) \star_5 W_{\ell}^{\mathbf{i}}. \quad (34)$$

Since we expect the advection velocity, normalized to the grid size, to be higher in the velocity advection step, we here restrict the shift to a maximum of two grid cells, i.e. we construct weights for $\ell \in \{-3, -2, -1, 0, 1, 2\}$ for the three-point stencil with three weights being zero for each coefficient.

The Hadamard product in (34) can be implemented as in the position step. The index shift is now along a direction that is compressed by the low-rank format. Fortunately, $f_{i-2} \in \mathbb{H}$ can be easily obtained from $f_i \in \mathbb{H}$ by simply shifting the rows of the factor matrix \mathbf{U} that belongs to the respective velocity space direction by two rows. Let $(\mathbf{U}_k)_i$ be the k th row vector of the factor matrix of f_i that belongs to the updated direction and $(\mathbf{U}_k)_{i-2}$ be the k th row vector of the respective factor matrix of f_{i-2} , then

$$(\mathbf{U}_k)_{i-2} = (\mathbf{U}_{k-2})_i \quad \forall k \in \{3, \dots, N_j\}, \quad (35)$$

where N_j is the number of cells in the updated direction. The shift of rows can be performed for all k if one chooses appropriate boundary conditions. In order to make sure that no particles are lost or created at the velocity space borders, we implement zero-flux boundary conditions. This can be achieved by setting in the factor matrices of the fluxes $\Phi_{i\pm 1} \in \mathbb{H}$ rows associated with the upper and lower limit of velocity space to zero such that there is no flux out of the border cells (and also no flux from outside of the velocity space limit).

3.6. Dual Solver for Conservation of Particle Density

Every truncation of the distribution function is accompanied by a small error which breaks the conservation properties that a Vlasov scheme can have without low-rank approximation. In particular, the low-rank version of the PFC scheme does no longer conserve mass. This is of course problematic for the physical reliability of the simulation, but also for the interplay of the Vlasov solver and the Maxwell solver. For the solution of Maxwell's equations we employ the finite-difference time-domain (FDTD) method. The involved staggered grid guarantees $\nabla \cdot \mathbf{B} = 0$. However, Gauss's law $\nabla \cdot \mathbf{E} = \rho/\epsilon_0$ will not be fulfilled

when the charge density is not conserved. A simple rescaling of f before the Maxwell step in order to conserve total charge density does improve the situation but is no sufficient solution—there are still local errors in ρ .

Algorithm 1: Time stepping of the low-rank Vlasov-Maxwell solver with moment fitting

Initial half step of the Maxwell solver

Time Step

Calculate second moment \mathcal{P}^n from f^n

Full Vlasov Leapfrog Step to advance to f^{n+1}

Calculate \mathcal{P}^{n+1} from f^{n+1}

Interpolate linearly to get $\mathcal{P}^{n+1/2}$

Full Runge-Kutta Fluid Step (input \mathcal{P} at appropriate times)

Moment Fitting

Calculate mean velocity \mathbf{u}_V from f

Artificial advection step with advection velocity $\mathbf{u}_V - \mathbf{u}_F$ to
enforce $\mathbf{u}_V = \mathbf{u}_F$

Calculate density n_V from f

Multiply f by n_F/n_V to conserve mass

end

Full step of the Maxwell solver

end

To conserve mass in the low-rank Vlasov solver, the advection scheme is combined with a partial differential equation (PDE) fluid solver using moment fitting [27, 28, 2]. The idea behind such a dual Vlasov solver is to transfer desirable properties that a fluid scheme has—here the conservation of mass and a good representation of Gauss’s law—to a Vlasov scheme which is missing those properties. Both the Vlasov solver and a fluid solver with kinetic input operate at the same time. When the fluid equations (3) and (4) are closed with help of the kinetic second moment \mathcal{P} obtained from the distribution function, they yield kinetically exact solutions for the density n_s and the mean velocity \mathbf{u}_s . Since the fluid solver conserves mass and fulfills the continuity equation independent of the conservation properties associated with \mathcal{P} , its kinetic solutions for n_s and \mathbf{u}_s can be used to correct the respective moments in the distribution function. This way, the resulting low-rank dual Vlasov solver can conserve mass and take Gauss’s law into account. In the dual Vlasov solver in [2] the distribution function was corrected by an exchange of the ten moment Maxwellian part of the distribution function with the ten moment Maxwellian obtained from the fluid solver. Thus, the information from the first three fluid equations can be utilized so that energy is corrected and conserved. In low-rank format this is not possible at good performance because the ten moment Maxwellian mixes two velocity space directions and therefore does not separate. It cannot be constructed directly in low-rank format and a truncation starting from the full tensor in each time step is much too costly. However, density and mean velocity

can easily be corrected. Here, the fluid solver utilizes a centrally weighted essentially non-oscillating (CWENO) method [29] and the third-order Runge-Kutta scheme in [30]. A time step of the dual low-rank Vlasov solver, as implemented, is described in Algorithm 1. First, a step of the low-rank Vlasov scheme is performed, followed by a step of the fluid scheme with input from the distribution function. The electric and magnetic fields obtained from the FDTD Maxwell solver are linearly interpolated from the staggered grid to the cell centers where they are needed by the plasma solvers. After the plasma solver steps, mean velocity is corrected by an artificial advection step and density is corrected by rescaling the distribution function.

As mentioned, this version of the moment fitting uses a four moment fluid solver where the hierarchy of fluid equations is closed at the momentum equation (4) using the second moment tensor \mathcal{P} obtained from the distribution function. The density of the stand-alone low-rank Vlasov solver is not conserved and is therefore corrected by the solution from the PDE fluid solver. Here, we correct the mean velocity not via an exchange of Maxwellians as in [2], but through an artificial advection step which moves the Vlasov solution towards the solution from the PDE solver. This method was introduced in [27] for spatial coupling of Vlasov and fluid models. The artificial advection step in velocity space is performed using the same scheme and interpolation as the regular advection steps described in Sec. 3.4 and Sec. 3.5. For a non-positive scheme like the low-rank scheme here, the advection method has the advantage that it does not introduce additional negativity caused by the exchange of Maxwellians. Since the four moment fluid solver does not yield a solution for the energy tensor, energy is not included in moment fitting and total energy is not conserved in the resulting low-rank dual Vlasov solver. However, the low-rank method allows much higher velocity space resolutions than the full grid solver and therefore also has less issues with numerical heating. The design of an energy-conserving low-rank solver will be an important aspect of future work in this direction.

4. Landau Damping

Landau damping is the predominant wave damping mechanism in collisionless plasmas. Because it is a kinetic effect that cannot easily be reproduced in fluid models and because an analytic solution is known for the linear regime, it has become a standard test case for kinetic plasma solvers. A static and spatially uniform neutralizing ion background is assumed and as the initial condition for the electron distribution function we use

$$f_{e,0}(\mathbf{x}, \mathbf{v}) = \frac{1}{(2\pi)^{3/2}} e^{-\frac{|\mathbf{v}|^2}{2}} \left(1 + \alpha \sum_{j=1}^3 \cos(k_j x_j) \right) \quad (36)$$

which is a perturbed Maxwell distribution in three dimensions. The setup is electrostatic and the normalization is given by: Time in units of the inverse electron plasma frequency $\omega_{p,0}^{-1}$, length in units of the electron Debye length

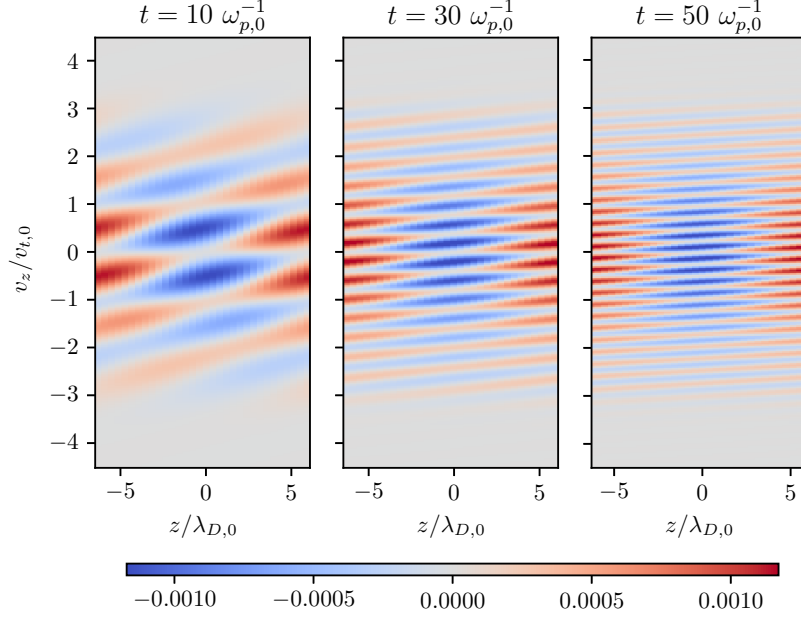


Figure 2: Filamentation of the distribution function in three-dimensional Landau damping. Shown is $f(t) - f(t=0)$ in the $z - v_z$ phase-space plane at $x = y = v_x = v_y = 0$.

$\lambda_{D,0}$, velocity in units of the electron thermal velocity $v_{t,0}$, mass in units of the electron mass m_e , temperature in units of the initial electron temperature T_0 , charge in units of the ion charge q_i and vacuum permittivity $\epsilon_0 = 1$. Here, it is $k_j = 0.5 \lambda_{D,0}^{-1}$ for all j and the perturbation is set to $\alpha = 0.01$. The physical domain goes from $x_j = -2\pi \lambda_{D,0}$ to $x_j = 2\pi \lambda_{D,0}$ and the velocity space from $v_j = -4.5 v_{t,0}$ to $v_j = 4.5 v_{t,0}$ in each direction j . Speed of light is set to $10 v_{t,0}$. The fields are evolved by the Maxwell solver (despite the electrostatic nature of the problem) in order to demonstrate that the presented six-dimensional Vlasov–Maxwell scheme can capture electrostatic Landau damping accurately.

The three-dimensional initialization that we chose separates in velocity space and is therefore perfectly suited for the low-rank solver. We perform a simulation with a resolution of 32^3 in position space and 256^3 in velocity space. Due to the separability it is sufficient to use rank one so that there is a lossless compression of the distribution function to $1/20\,000$ of the full-grid data. The simulation can be run on a single modern CPU whereas the full-grid version would require a large supercomputer. Admittedly, this is the most ideal situation for the low-rank solver, but it is nevertheless worthwhile to demonstrate that the high velocity space resolution can be utilized despite the massively reduced degrees of freedom. This is shown in Fig. 2 where the deviation of the distribution function from the initial value is given for different times. Due to the different speeds of the particles in the Maxwell distribution, increasingly small scale structures

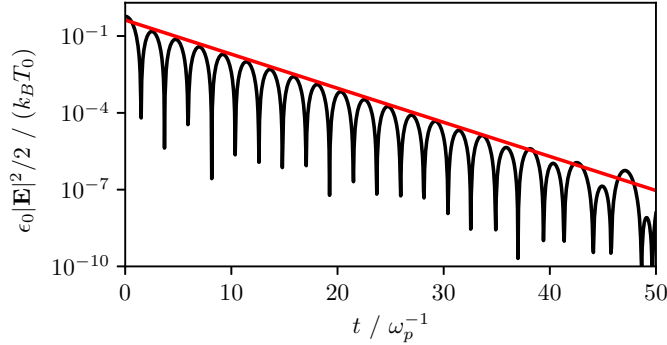


Figure 3: Damping of the electric wave energy in three-dimensional Landau damping. Red: Analytic damping rate.

develop which is known as the filamentation of the distribution function. The filamentation is accurately resolved by the high velocity space resolution despite the compression. In Fig. 3 the damping of the electric energy is shown next to the analytic damping rate of $\gamma = 0.1533\omega_{p,0}$. The simulation matches this rate, only at later times the discretization error in position space begins to dominate the small remaining perturbation which is expected at a resolution of 32^3 . Within the simulated time span there is no recurrence effect which would occur if the filamentation became finer than the velocity resolution.

5. Orszag-Tang Turbulence

In this section we compare the low-rank Vlasov solver to the full grid version in a well-known plasma turbulence setup, the Orszag-Tang vortex. We choose parameters as in [31] apart from a lower ion-electron mass ratio (here $m_i/m_e = 25$). The initial magnetic field is $B_y = -\delta_B \sin(2\pi z/L)$, $B_z = \delta_B \sin(4\pi y/L)$ and $B_x = 1B_0$ and the velocities are $u_{y,s} = -\delta_u \sin(2\pi z/L)$, $u_{z,s} = \delta_u \sin(2\pi y/L)$, $u_{x,i} = 0$ and $u_{x,e} = -\frac{2\pi}{L}\delta_B\mu_0(2\cos(4\pi y/L) + \cos(2\pi z/L))$. The perturbation has a magnitude of $\delta_u = 0.2v_{A,0}$ and $\delta_B = 0.2B_0$. The current in x -direction is carried by the electrons. The electric field is $E_y = -\delta_u B_0 \sin(2\pi y/L)$, $E_z = -\delta_u B_0 \sin(2\pi z/L)$ and $E_x = 0$. The initial density is uniform $n_s = n_0$ apart from a small perturbation added to same parts to the electron and ion densities in order to satisfy Gauss's law. The temperature ratio is $T_i/T_e = 1$ with $\beta_i = 2\mu_0 n_0 k_B T_i / B_0^2 = 0.1$ and the speed of light is $c = 18.174v_{A,0}$. The distribution function is initialized as a Maxwellian distribution based on the aforementioned quantities. The spatial resolution is chosen as 128^2 in order to resolve electron inertial length in the periodic domain of size $L_y = L_z = L = 8\pi d_{i,0}$. The velocity space extends from $-9v_{A,0}$ to $9v_{A,0}$ for the electrons and from $-2v_{A,0}$ to $2v_{A,0}$ for the ions.

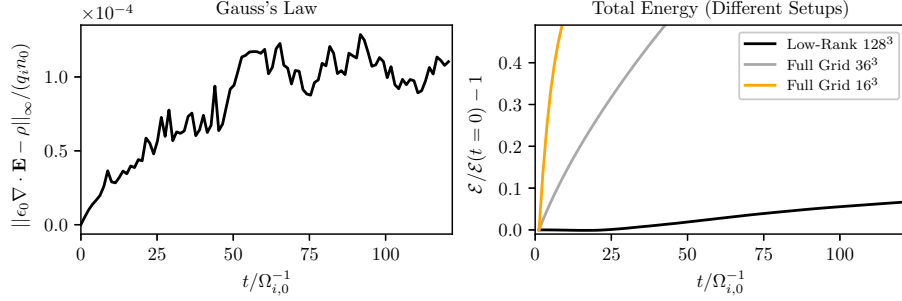


Figure 4: Evolution of the error in Gauss's law and total energy conservation over time in the Orszag-Tang turbulence simulation.

In electromagnetic setups like Orszag-Tang turbulence (and also GEM reconnection in the next section) we choose the following normalization: Length in units of the ion inertial length $d_{i,0}$ based on density n_0 , velocity in units of the ion Alfvén velocity $v_{A,0}$ based on the magnetic field B_0 , time in units of the inverse of the ion cyclotron frequency $\Omega_{i,0}^{-1}$, mass in units of the ion mass m_i , electric charge in units of the ion charge q_i , vacuum permeability $\mu_0 = 1$ and Boltzmann constant $k_B = 1$.

The low-rank simulation uses a velocity space resolution of 128^3 cells and rank $r = 8$. This results in a compression of 1:574, i.e. a compression to less than 0.18% of the full data. Compared to a full grid simulation that is resolved by 128^3 cells, the low-rank simulation achieves a speed-up by a factor of 70. Here, we compare the low-rank simulation (i) to a full grid simulation that takes the same computational time (wall time) per step and (ii) to a full grid simulation that uses the same degrees of freedom (DOF). The respective velocity space resolutions are 36^3 (same wall time) and 16^3 (same DOF). Note that the implementation of the hierarchical Tucker algorithms used by the low-rank solver still has lots of room for performance improvement, for example by avoiding unnecessary copy operations and allocations/deallocations. The full grid solver on the other hand is highly optimized already. For an otherwise fair comparison, we utilize in the full-grid simulations the advantages that an explicitly available grid brings: The positivity preserving limiters are turned on and the velocity splitting is realized via the backsubstitution method [32]. The full grid simulations are performed with the *muphy2* multiphysics plasma simulation code [2, 33].

First, we will discuss some features of the low-rank solver. The low-rank approximation leads to non-conservation of the distribution function and in consequence non-conservation of total mass. This can be corrected by means of moment fitting as presented in Sec. 3.6. The mass correction on basis of a fluid solver with kinetic input enables the low-rank Vlasov-Maxwell solver to self-consistently take Gauss's law into account, without the need for divergence cleaning which was used for example in [15]. The FDTD Maxwell solver evolves

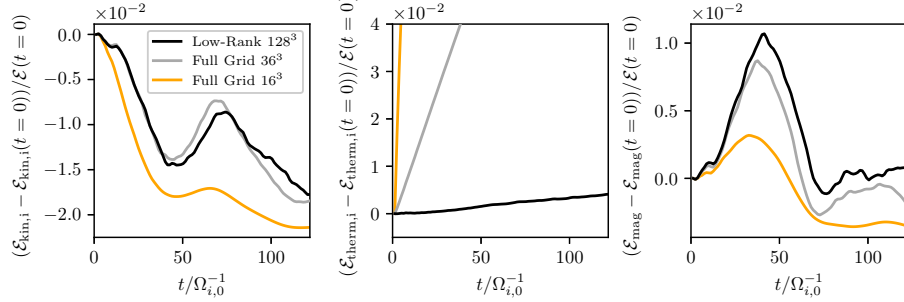


Figure 5: Change of energy partition between ion kinetic energy, ion thermal energy and magnetic energy in the low-rank Vlasov solver compared to the full grid version at the same wall time (36^3) and the same degrees of freedom (16^3).

the fields according to Ampère’s law and Faraday’s law. These two equations are sufficient if $\nabla \cdot \mathbf{B} = 0$ and Gauss’s law $\nabla \cdot \mathbf{E} = \rho/\epsilon_0$ are fulfilled initially and the plasma solver satisfies some requirements: It needs to provide the appropriate current density as an input to Ampère’s law on the staggered grid and has to fulfill the continuity equation for charge. The current density on the staggered grid can be provided by the reconstruction that is performed during the solution of the fluid equations, and the continuity equation is fulfilled in form of the first fluid equation. In Fig. 4 the errors in Gauss’s law (left) and in energy conservation (right) are shown. As becomes apparent, there is still a small error present in Gauss’s law which is related to the different time-stepping in the fluid solver and the Maxwell solver. In order to further improve the representation of Gauss’s law, the FDTD Maxwell solver could for example be replaced by a solver that uses Runge-Kutta time-stepping like the fluid solver. However, the FDTD method has several desirable properties (it is energy-conserving, symplectic, robust and stable and has low numerical dissipation) and for many applications the obtained accuracy in Gauss’s law is sufficient.

As discussed, the current implementation of the low-rank solver, as well as the positivity preserving full grid scheme it is based on, are not energy-conserving. Analytically, total energy $\mathcal{E} = \int \sum_s (m_s n_s |\mathbf{u}_s|^2/2 + n_s k_B T_s) + |\mathbf{B}|^2/(2\mu_0) + \epsilon_0 |\mathbf{E}|^2/2 \, d\mathbf{x}$ is conserved in the Vlasov-Maxwell system of equations (in for example an infinite or periodic domain). The high velocity space resolutions that are possible with the low-rank solver lead to lower errors in energy conservation as shown in Fig. 4. There, the low-rank solver with resolution 128^3 , $r = 8$ is compared to the full grid solver at resolutions of 36^3 (same computational time) and 16^3 (same degrees of freedom). The significantly reduced numerical heating in the low-rank solver is a consequence of improved numerical accuracy in addition to the improved physical accuracy that the higher resolution provides. Nevertheless, a more exact energy conservation is desirable and improvements to the low-rank solver in this direction are necessary in the future.

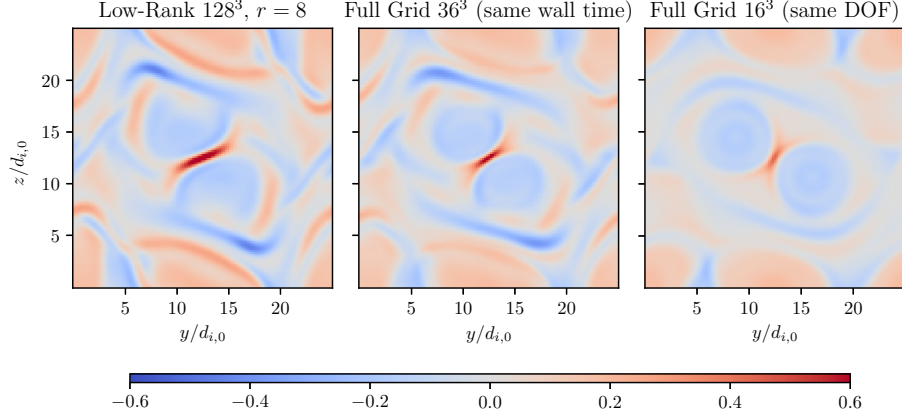


Figure 6: Out-of-plane current density at $t = 62.83 \Omega_{i,0}$ in the low-rank simulation and comparable full grid simulations.

The comparison between the three configurations is continued in Fig. 5 where the evolution of the energy partition is shown, in particular the change of ion kinetic energy $\mathcal{E}_{\text{kin},i} = \int m_i n_i |\mathbf{u}_i|^2 / 2 \, d\mathbf{x}$, ion thermal energy $\mathcal{E}_{\text{therm},i} = \int n_i k_B T_i \, d\mathbf{x}$ and magnetic energy $\mathcal{E}_{\text{mag}} = \int |\mathbf{B}|^2 / (2\mu_0) \, d\mathbf{x}$ over time. The results from the highly-resolved low-rank simulation are in good agreement with published results from fully kinetic simulations [31, 2] whereas in the comparable full grid simulations the numerical heating of the PFC Vlasov scheme in combination with low resolutions contaminates the results. The same holds for the spatial structure of the turbulent fields shown at the example of the out-of-plane current density j_x in Fig. 6. Due to numerical dissipation, the full grid simulations miss details that the low-rank simulation captures. There is good agreement of the current density's spatial structure with the aforementioned published PIC and Vlasov results in the case of the low-rank solver. This indicates that despite the exceptionally high compression no substantial kinetic information is lost.

6. GEM Reconnection

A standard test setup for magnetic reconnection is given by the Geospace Environmental Modeling (GEM) challenge [34]. There, the initial configuration is a Harris sheet with density $n_s = n_0 \text{sech}^2(z/\lambda) + n_b$ and magnetic field $B_y = \tanh(z/\lambda)B_0 + \delta B_y$, $B_z = \delta B_z$. The background density is $n_b = 0.2 n_0$ and the half-width of the current sheet is $\lambda = 0.5 d_{i,0}$. The uniform temperature is defined according to $n_0 k_B (T_e + T_i) = B_0^2 / (2\mu_0)$, $T_i / T_e = 5$. The reconnection process is initiated by a perturbation $\delta B_y = -\psi_0 \pi / L_z \cos(2\pi y / L_y) \sin(\pi z / L_z)$, $\delta B_z = \psi_0 2\pi / L_y \sin(2\pi y / L_y) \cos(\pi z / L_z)$ with $\psi_0 = 0.1 B_0 d_{i,0}$. The magnetic field gradients are associated with a current density which is distributed among electrons and ions according to $u_{x,i} / u_{x,e} = T_i / T_e$. The ion to electron mass ratio

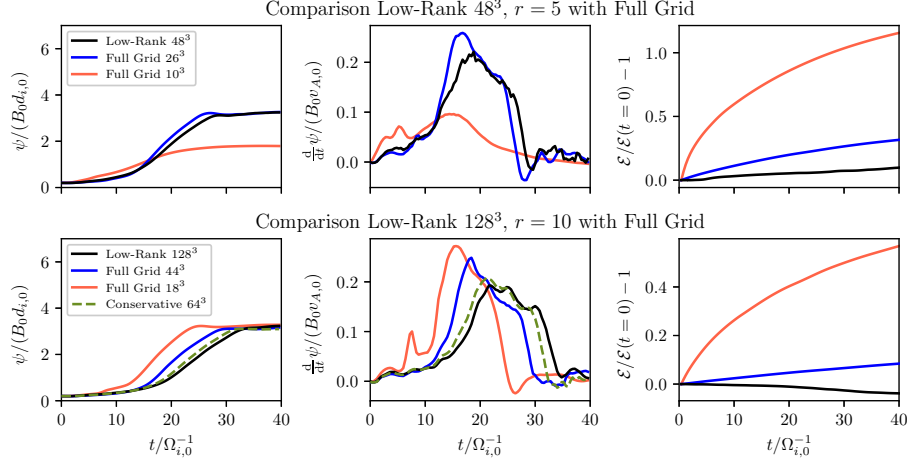


Figure 7: Comparison of solver configurations: Reconnected flux Ψ , reconnection rate $\frac{d}{dt}\Psi$, and the error in energy conservation over time in simulations of magnetic reconnection.

is $m_i/m_e = 25$ and the speed of light is $c = 20 v_{A,0}$. A Maxwellian distribution computed from aforementioned quantities serves as the initial condition for the particle distribution function. We resolve the domain $L_y \times L_z = 8\pi d_{i,0} \times 4\pi d_{i,0}$ by 256×128 cells. The boundary conditions are periodic in y -direction, at the z -boundaries there are reflecting walls for particles that are conducting for fields and in x -direction there is no spatial variation. We simulate only the lower right quarter of the domain and utilize symmetries of the setup in order to save computational time. Electron velocity space ranges from $-10 v_{A,0}$ to $10 v_{A,0}$ and ion velocity space from $-5 v_{A,0}$ to $5 v_{A,0}$.

In this reconnection setup we test the low-rank Vlasov solver with different ranks against comparable full grid solutions with the same wall time and degrees of freedom, respectively, as well as a well-resolved full grid Vlasov simulation that uses an energy conserving scheme. The first low-rank configuration uses 48^3 cells in velocity space and a rank $r = 5$ which corresponds to a compression of 1:127 (0.78% of the full data). It is compared to full grid simulations with a resolution of 10^3 for the same degrees of freedom and 26^3 for the same wall time. The second low-rank configuration is resolved by 128^3 cells with rank $r = 10$. Then the compression is 1:424 (0.24% of the full data) so that we achieve a speed-up by a factor of 40 compared to a full grid simulation with 128^3 cells. Here, the same degrees of freedom and same wall time counterparts on the full grid use 18^3 cells and 44^3 cells. Finally, we also performed a full grid simulation that uses the positivity preserving and energy conserving dual Vlasov solver from [2] and a resolution of 64^3 cells.

These different configurations are compared in Fig. 7 concerning the evolution of reconnected magnetic flux Ψ and reconnection rate $\frac{d}{dt}\Psi$ next to the error in energy conservation. The reconnected flux is here the integral over B_z at

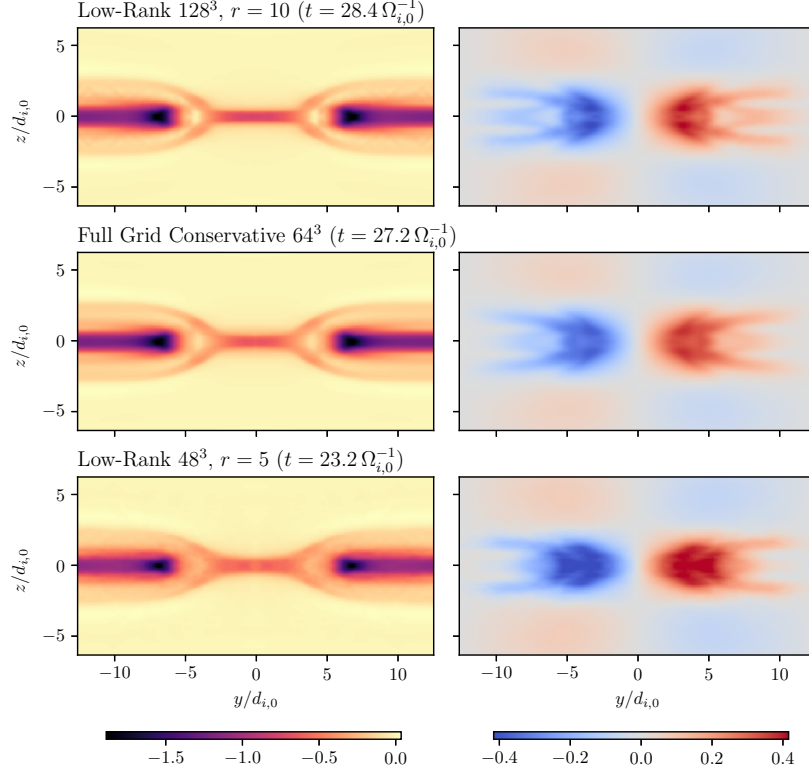


Figure 8: Low-rank and full grid solutions for the out-of-plane current density $j_x/(n_0 v_{A,0})$ (left) and ion outflow velocity $u_{y,i}/v_{A,0}$ (right) compared between different ranks and the full grid.

$z = 0$ from the center to the right border of the domain $\Psi = \int_0^{4\pi} B_z(y, z=0) dy$. The upper row in Fig. 7 shows the $r = 5$ case and the corresponding full grid runs. At the same degrees of freedom as the low-rank simulation, the full grid solver fails to appropriately represent the reconnection process. The better velocity space resolution furthermore results in a lower peak reconnection rate. In the lower row the results from the $r = 10$ simulation are shown. Again there is the tendency that the peak reconnection rate decreases at better velocity space resolutions. The qualitative development is similar between the 128^3 low-rank simulation and the 64^3 energy conserving full grid simulation. There is some numerical cooling in the low-rank simulation that leads to a later onset of reconnection. The slightly lower peak reconnection rate in the low-rank case likely results from the better resolution.

The effect of compression (low-rank approximation) can best be seen in a direct comparison of physical quantities between simulations of different rank and a full-grid simulation. For this purpose, various quantities are shown in the Figures 8–10 for the $r = 10$ low-rank simulation (128^3), the energy conserving

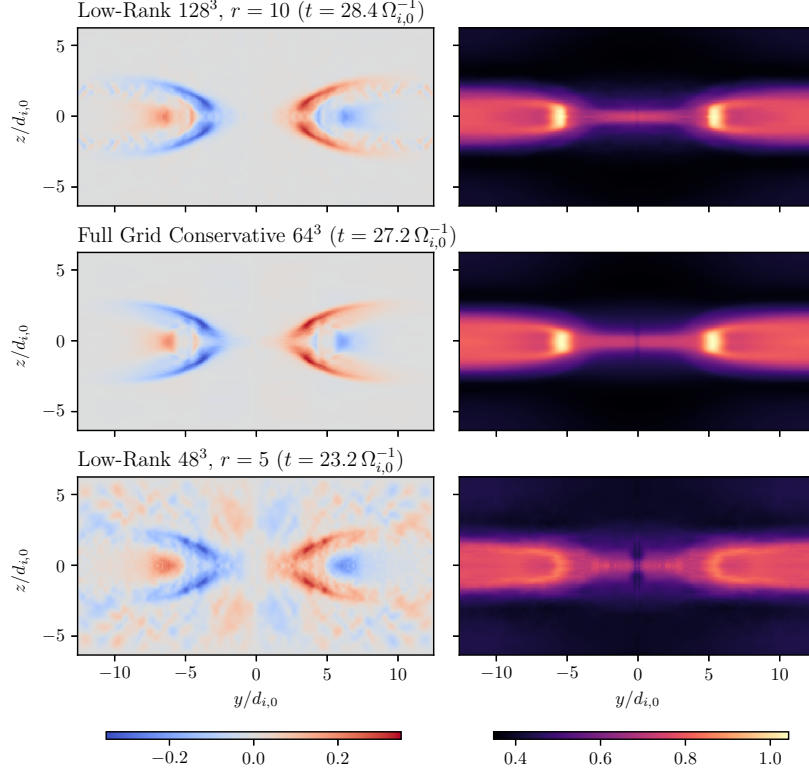


Figure 9: Low-rank and full grid solutions for the hall electric field $E_y/(B_0 v_{A,0})$ (left) and the ion temperature $T_i/(m_i v_{A,0}^2/k_B)$ (right).

full grid simulation (64^3) and the $r = 5$ low-rank simulation (48^3). The snapshots are taken at times where $\Psi = 2.5 B_0 d_{i,0}$ so that the reconnection is in a similar state. The reconnection current sheet density j_x in Fig. 8 typically gives a good overview over the reconnection as it visualizes both the X- and the O-line. There is excellent agreement between the three configurations which is especially encouraging in the $r = 5$ case which uses very few degrees of freedom (870 DOF for the velocity space). On the right hand side of Fig. 8 the ion outflow velocity $u_{y,i}$ is shown. It is mostly identical in the $r = 10$ and full grid cases, but somewhat overestimated by the $r = 5$ run. The low-rank $r = 10$ simulation yields a slightly sharper and more detailed picture than the full grid simulation.

The Hall reconnection field E_y is given in Fig. 9 next to the ion temperature T_i . In both quantities, but especially in the electric field, two characteristics of the low-rank solver are visualized in the $r = 5$ case. First, a low rank is associated with noise caused by the round-off error during the truncation of SVDs. Second, because the solver does not preserve positivity of the distribu-

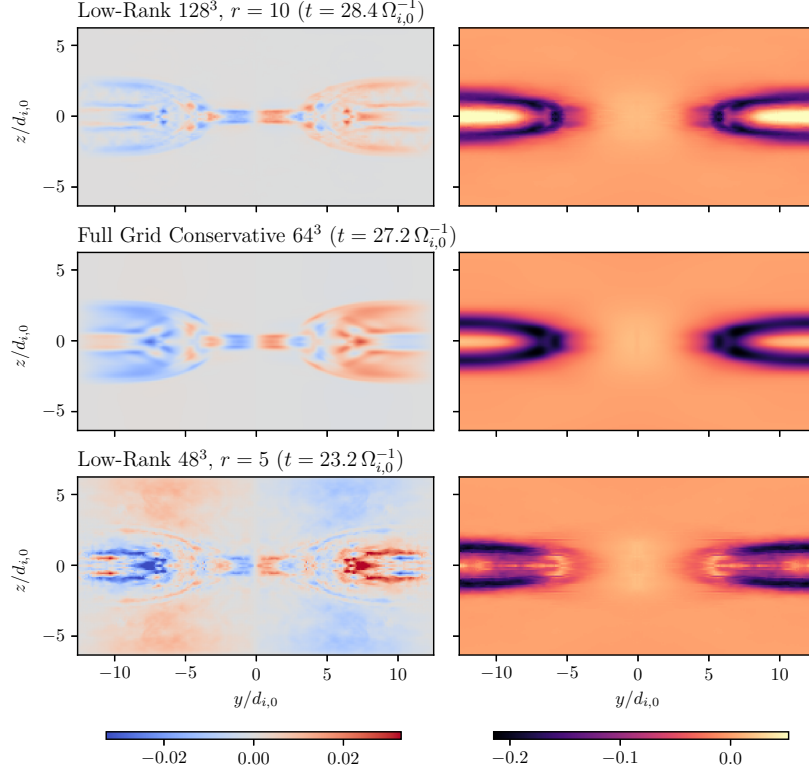


Figure 10: Low-rank and full grid solutions for the electron heat flux component $Q_{xy,e}/(m_i n_0 v_{A,0}^3)$ and the ion heat flux component $Q_{xy,i}/(m_i n_0 v_{A,0}^3)$.

tion function, numerical oscillations may be present. However, both effects are relatively small in this case. In the $r = 10$ case there is almost no noise, but naturally some numerical oscillations are visible in the electric field. Ion temperature matches for the $r = 10$ and the full grid simulation and its structure is also caught by the $r = 5$ simulation.

Finally, two heat flux components—one for the electrons and one for the ions—are shown in Fig. 10. The components of the heat flux are very sensitive to the representation of the velocity distribution and are a good indicator of how much information is lost due to the compression of the distribution function. It can be seen that the detailed structure in the $Q_{xy,e}$ component agrees accurately between the $r = 10$ low-rank solution and the full grid solution. Even the $r = 5$ solution captures the heat flux very well although the magnitude is overestimated in some regions and the heat flux is overall somewhat noisy. Nevertheless, this shows a very important and encouraging characteristic of the low-rank solutions: At low ranks they yield a less accurate picture of the correct physics rather than an accurate picture of incorrect (non-kinetic) physics as

for example fluid approximations do. At high ranks on the other hand, almost no kinetic information is lost. Similar conclusions can also be drawn from the shown ion heat flux component $Q_{xyy,i}$. Again, there is good agreement between the $r = 10$ low-rank simulation and the conservative full grid simulation and a decent representation in the $r = 5$ case.

7. Conclusions

A low-rank solver for the full six-dimensional Vlasov-Maxwell equations was presented and tested in benchmark problems of plasma turbulence and magnetic reconnection. Massive compression of the distribution function to for example 1/500 of the full data is possible without significant loss of information. With the current version of the code speed-ups of up to 70 have been achieved in realistic setups. Compared to full grid simulations using the same numerical scheme and the same computational time or degrees of freedom, the low-rank simulations yield much more accurate results. The dual Vlasov (moment fitting) method—where the Vlasov solver is complemented by a fluid solver with kinetic moment input—makes the low-rank solver mass conservative and enables a good representation of Gauss’s law.

Generally, the development of low-rank Vlasov solvers is still a rather new field of research with enormous potential. One of the most important extensions of the low-rank solver would be the introduction of limiters to preserve the positivity of the compressed distribution function. Equally important is a good conservation of total energy and momentum.

The implementation of the low-rank solver is fully parallelized using MPI and a domain decomposition approach and scales well on large HPC CPU clusters. It would be desirable to be able to utilize GPUs which is possible but highly non-trivial [35]. The currently used implementation of the hierarchical Tucker operations serves more as a prototype implementation and leaves room for optimizations and performance improvements since no special care has been taken so far to avoid data copying and allocations/deallocations.

In the future, the rank of the approximation may depend on position space so that high ranks are only used where they are required to capture physical effects. With efficient load balancing such an approach can lead to significant performance gains in large-scale simulations.

Acknowledgments

We gratefully acknowledge the Gauss Centre for Supercomputing e.V. (www.gauss-centre.eu) for funding this project by providing computing time through the John von Neumann Institute for Computing (NIC) on the GCS Supercomputer JUWELS at Jülich Supercomputing Centre (JSC). Computations were conducted on JUWELS-booster [Jülich Supercomputing Centre, 2019] and on the DaVinci cluster at TP1 Plasma Research Department. F.A. was supported by the Helmholtz Association (VH-NG-1239).

References

- [1] H. Schmitz, R. Grauer, Kinetic Vlasov simulations of collisionless magnetic reconnection, *Physics of Plasmas* 13 (9) (2006) 092309. doi:10.1063/1.2347101.
- [2] F. Allmann-Rahn, S. Lautenbach, R. Grauer, An energy conserving Vlasov solver that tolerates coarse velocity space resolutions: Simulation of MMS reconnection events, *arXiv e-prints* (2021) arXiv:2109.06743.
- [3] O. Pezzi, H. Liang, J. L. Juno, P. A. Cassak, C. L. Vásconez, L. Sorriso-Valvo, D. Perrone, S. Servidio, V. Roytershteyn, J. M. TenBarge, W. H. Matthaeus, Dissipation measures in weakly collisional plasmas, *Monthly Notices of the Royal Astronomical Society* 505 (4) (2021) 4857–4873. doi:10.1093/mnras/stab1516.
- [4] J. Juno, A. Hakim, J. TenBarge, E. Shi, W. Dorland, Discontinuous Galerkin algorithms for fully kinetic plasmas, *Journal of Computational Physics* 353 (2018) 110 – 147. doi:10.1016/j.jcp.2017.10.009.
- [5] O. Pezzi, G. Cozzani, F. Califano, F. Valentini, M. Guarrasi, E. Camporeale, G. Brunetti, A. Retinò, P. Veltri, ViDA: a Vlasov–DARwin solver for plasma physics at electron scales, *Journal of Plasma Physics* 85 (5) (2019) 905850506. doi:10.1017/S0022377819000631.
- [6] I. Pusztai, J. Juno, A. Brandenburg, J. M. TenBarge, A. Hakim, M. Francisquez, A. Sundström, Dynamo in weakly collisional nonmagnetized plasmas impeded by Landau damping of magnetic fields, *Phys. Rev. Lett.* 124 (2020) 255102. doi:10.1103/PhysRevLett.124.255102.
- [7] K. Kormann, A semi-lagrangian vlasov solver in tensor train format, *SIAM Journal on Scientific Computing* 37 (4) (2015) B613–B632. arXiv:https://doi.org/10.1137/140971270, doi:10.1137/140971270. URL https://doi.org/10.1137/140971270
- [8] U. Schollwöck, The density-matrix renormalization group in the age of matrix product states, *Annals of Physics* 326 (2011) 96–192. doi:https://doi.org/10.1016/j.aop.2010.09.012. URL https://www.sciencedirect.com/science/article/pii/S0003491610001752
- [9] J. I. Cirac, D. Pérez-García, N. Schuch, F. Verstraete, Matrix product states and projected entangled pair states: Concepts, symmetries, theorems, *Rev. Mod. Phys.* 93 (2021) 045003. doi:10.1103/RevModPhys.93.045003. URL https://link.aps.org/doi/10.1103/RevModPhys.93.045003
- [10] M. Bachmayr, R. Schneider, A. Uschmajew, Tensor networks and hierarchical tensors for the solution of high-dimensional partial differential equations, *Foundations of Computational Mathematics* 16 (6) (2016) 1423–1472. doi:10.1007/s10208-016-9317-9. URL https://doi.org/10.1007/s10208-016-9317-9

- [11] L. Grasedyck, D. Kressner, C. Tobler, A literature survey of low-rank tensor approximation techniques, *GAMM-Mitteilungen* 36 (1) (2013) 53–78.
arXiv:<https://onlinelibrary.wiley.com/doi/pdf/10.1002/gamm.201310004>,
doi:<https://doi.org/10.1002/gamm.201310004>.
URL <https://onlinelibrary.wiley.com/doi/abs/10.1002/gamm.201310004>
- [12] V. Ehrlacher, D. Lombardi, A dynamical adaptive tensor method for the vlasov–poisson system, *Journal of Computational Physics* 339 (2017) 285 – 306. arXiv:<https://doi.org/10.1016/j.jcp.2017.03.015>.
- [13] L. Einkemmer, C. Lubich, A low-rank projector-splitting integrator for the vlasov–poisson equation, *SIAM Journal on Scientific Computing* 40 (5) (2018) B1330–B1360. arXiv:<https://doi.org/10.1137/18M116383X>,
doi:10.1137/18M116383X.
URL <https://doi.org/10.1137/18M116383X>
- [14] L. Einkemmer, C. Lubich, A quasi-conservative dynamical low-rank algorithm for the vlasov equation, *SIAM Journal on Scientific Computing* 41 (5) (2019) B1061–B1081. arXiv:<https://doi.org/10.1137/18M1218686>,
doi:10.1137/18M1218686.
URL <https://doi.org/10.1137/18M1218686>
- [15] L. Einkemmer, A. Ostermann, C. Piazzola, A low-rank projector-splitting integrator for the vlasov–maxwell equations with divergence correction, *Journal of Computational Physics* 403 (2020) 109063. doi:<https://doi.org/10.1016/j.jcp.2019.109063>.
- [16] F. Cassini, L. Einkemmer, Efficient 6D Vlasov simulation using the dynamical low-rank framework Ensign, arXiv e-prints (2021) arXiv:2110.13481.
- [17] S. Dolgov, M. Stoll, Low-rank solution to an optimization problem constrained by the navier–stokes equation, *SIAM Journal on Scientific Computing* 39 (1) (2017) A255–A280. arXiv:<https://doi.org/10.1137/15M1040414>,
doi:10.1137/15M1040414.
URL <https://doi.org/10.1137/15M1040414>
- [18] L. Einkemmer, A low-rank algorithm for weakly compressible flow, *SIAM Journal on Scientific Computing* 41 (5) (2019) A2795–A2814. arXiv:<https://doi.org/10.1137/18M1185417>,
doi:10.1137/18M1185417.
URL <https://doi.org/10.1137/18M1185417>
- [19] W. Hackbusch, S. Kühn, A new scheme for the tensor representation, *Journal of Fourier Analysis and Applications* 15 (5) (2009) 706–722. arXiv:<https://doi.org/10.1007/s00041-009-9094-9>,
doi:10.1007/s00041-009-9094-9.

- [20] L. Grasedyck, Hierarchical singular value decomposition of tensors, *SIAM Journal on Matrix Analysis and Applications* 31 (4) (2010) 2029–2054.
arXiv:<https://doi.org/10.1137/090764189>, doi:10.1137/090764189.
URL <https://doi.org/10.1137/090764189>
- [21] E. Schmidt, Zur theorie der linearen und nichtlinearen integralgleichungen, *Mathematische Annalen* 63 (4) (1907) 433–476. doi:10.1007/BF01449770.
- [22] C. Eckart, G. Young, The approximation of one matrix by another of lower rank, *Psychometrika* 1 (3) (1936) 211–218.
arXiv:<https://doi.org/10.1007/BF02288367>, doi:10.1007/BF02288367.
- [23] L. Mirsky, Symmetric gauge functions and unitarily invariant norms, *The Quarterly Journal of Mathematics* 11 (1) (1960) 50–59.
arXiv:<http://dx.doi.org/10.1093/qmath/11.1.50>, doi:10.1093/qmath/11.1.50.
- [24] D. Kressner, C. Tobler, Algorithm 941: Htucker—a matlab toolbox for tensors in hierarchical tucker format, *ACM Trans. Math. Softw.* 40 (3) (2014) 22:1–22:22. doi:10.1145/2538688.
- [25] C. Tobler, D. Kressner, Hierarchical tucker toolbox, URL: <https://anchp.epfl.ch/index-html/software/htucker/>, accessed: 2021-10-28. (2012).
- [26] F. Filbet, E. Sonnendrücker, P. Bertrand, Conservative numerical schemes for the Vlasov equation, *Journal of Computational Physics* 172 (1) (2001) 166 – 187. doi:10.1006/jcph.2001.6818.
- [27] M. Rieke, T. Trost, R. Grauer, Coupled Vlasov and two-fluid codes on GPUs, *Journal of Computational Physics* 283 (2015) 436 – 452. doi:10.1016/j.jcp.2014.12.016.
- [28] T. Trost, S. Lautenbach, R. Grauer, Enhanced conservation properties of Vlasov codes through coupling with conservative fluid models, *arXiv e-prints* (2017) arXiv:1702.00367.
- [29] A. Kurganov, D. Levy, A third-order semidiscrete central scheme for conservation laws and convection-diffusion equations, *SIAM Journal on Scientific Computing* 22 (4) (2000) 1461–1488. doi:10.1137/S1064827599360236.
- [30] C.-W. Shu, S. Osher, Efficient implementation of essentially non-oscillatory shock-capturing schemes, *Journal of Computational Physics* 77 (2) (1988) 439 – 471. doi:10.1016/0021-9991(88)90177-5.
- [31] D. Grošelj, S. S. Cerri, A. B. Navarro, C. Willmott, D. Told, N. F. Loureiro, F. Califano, F. Jenko, Fully kinetic versus reduced-kinetic modeling of collisionless plasma turbulence, *The Astrophysical Journal* 847 (1) (2017) 28. doi:10.3847/1538-4357/aa894d.

- [32] H. Schmitz, R. Grauer, Comparison of time splitting and backsubstitution methods for integrating Vlasov's equation with magnetic fields, *Comp. Phys. Comm.* 175 (2006) 86.
- [33] F. Allmann-Rahn, S. Lautenbach, R. Grauer, R. D. Sydora, Fluid simulations of three-dimensional reconnection that capture the lower-hybrid drift instability, *Journal of Plasma Physics* 87 (1) (2021) 905870115. doi:10.1017/S0022377820001683.
- [34] J. Birn, J. F. Drake, M. A. Shay, B. N. Rogers, R. E. Denton, M. Hesse, M. Kuznetsova, Z. W. Ma, A. Bhattacharjee, A. Otto, P. L. Pritchett, Geospace environmental modeling (GEM) magnetic reconnection challenge, *Journal of Geophysical Research: Space Physics* 106 (A3) (2001) 3715–3719. doi:10.1029/1999JA900449.
- [35] W. Boukaram, G. Turkiyyah, D. Keyes, Hierarchical matrix operations on gpus: Matrix-vector multiplication and compression, *ACM Trans. Math. Softw.* 45 (1). doi:10.1145/3232850.